Carbon isotope fractionation between CO_2 and carbon in silicate melts at high temperature

Hyunjoo Lee[1], Yves Moussallam[1,2], Cyril Aubaud[3], Giada Iacono-Marziano[4], Keiji Hammond[2], Denton Ebel[2].

[1] *Lamont-Doherty Earth Observatory, Columbia University, New York, USA*

[2] *American Museum of Natural History, Department of Earth and Planetary Sciences, NY 10024, New York, USA*

[3] *Université Paris Cité, Institut de Physique du Globe de Paris, CNRS, Laboratoire de Géochimie des Isotopes Stables, 1 rue Jussieu, F-75005 Paris, France*

[4] *ISTO, UMR 7327 Université d'Orléans-CNRS-BRGM, 1a rue de la Ferollerie, Orléans, France*

Corresponding author: Hyunjoo Lee; hl3507@columbia.edu

Keywords: carbon isotopes; carbon isotope fractionation factor; carbon species; $\delta^{13}C$-value

Abstract

The isotopic fractionation of carbon between CO_2 gas and silicate melts is a crucial parameter to understand the carbon cycle at the planetary scale that requires accurate quantification. In this study, we conducted experiments to determine the carbon isotope fractionation between CO_2 gas and carbon dissolved in silicate melt at 350-420 MPa and 1160-1225°C, across a range of melt compositions. A linear relationship emerges between the fractionation coefficient and the degree of polymerization of the melt (NBO/T; non-bridging oxygens per tetrahedral cation) with the fractionation coefficient increasing for depolymerized melts (e.g., basalt) and decreasing for polymerized melts (e.g., rhyolite):

$$1000\ln\alpha_{gas\text{-}melt}=2.847\times NBO/T+0.068\ (R^2=0.74)$$

or

$$1000\ln\alpha_{g\text{-}m}=-0.087\times(SiO_2+Al_2O_3)wt\%+7.968\ (R^2=0.74)$$

These equations enable the calculation of carbon fractionation coefficients in silicate melts, providing a mean to interpret $\delta^{13}C$-value measurements in natural volcanic gases and melts through forward and backward modelling of degassing paths from mantle to surface. The relationship is calibrated from NBO/T = 0 to 1, covering most major melt compositions. However, it is expected to stabilize and remain constant at NBO/T > 1. We hypothesize that the ratio of CO_3^{2-}/CO_2 dissolved in the melt is the key parameter behind this relationship. Carbon dissolved as CO_2 molecular transfers to the gas phase with a fractionation coefficient of 0 ‰ whilst carbon dissolved as CO_3^{2-} transfers with a fractionation coefficient of 2.9 ‰. Carbon isotopic fractionation might hence offer a window into carbon speciation in natural melts.

1. Introduction

Dissolved carbon in magmatic systems is an abundant volatile component that plays a crucial role in determining the initiation depth of partial melting (e.g., Dasgupta and Hirschmann, 2010) and physical properties of mantle melts (e.g., Gaillard et al., 2008; Yoshino et al., 2012). Carbon in the mantle exists in various forms, including diamond (e.g., Jaques et al., 1990), graphite (e.g., Pearson et al., 1994), and carbonate inclusions (e.g., Ionov et al., 1993), as well as fluid inclusions composed of CO_3^{2-}, CH_4, CO, and COS (e.g., Andersen and Neumann, 2001). Under lithospheric conditions (i.e., 0.5 to 4 GPa, below 2000 °C, and FMQ-1 to +3.5; Solomatova et al., 2020), carbon exists primarily in dissolved forms as either carbonate ion (CO_3^{2-}) or CO_2 molecular in silicate melts (e.g., Blank and Brooker, 1994; Brey and Green, 1976; Mysen et al., 1976). In the coexisting exsolved gas phase, carbon is predominantly found as CO_2, with lesser amounts of CO (Wardell et al., 2004).

The solubility of CO_2 in silicate melts has a significant positive correlation with depolymerization of the melt and total pressure. To describe the complex relationship between melt composition and CO_2 solubility, researchers have proposed a compositional parameter, Π, (Dixon, 1997; Shishkina et al., 2014) and NBO/T (Non-Bridging Oxygens per Tetrahedral Cations; Brooker et al., 2001), which reflects the ratio between the freely diffusing cations and the tetrahedral network, as a way of measuring the degree of melt polymerization. In addition, experiments have consistently shown that the CO_2 solubility decreases with decreasing pressure across a range of compositions, from felsic to ultramafic and from less than a hundred MPa to several GPa, respectively (e.g., Jendrzejewski et al., 1997; Shishkina et al., 2014; Stolper and Holloway, 1988). This positive correlation commonly leads to CO_2 saturation in the magma during its journey toward the surface, with very few examples to date of magmatic systems where CO_2-undersaturated melts have been identified (Javoy and Pineau, 1991; Saal et al., 2002; Michael and Graham, 2015; Le Voyer et al., 2017).

CO_2 has relatively low solubility among the major volatiles (H_2O-CO_2), for example, the maximum solubility of H_2O is 6 wt% and CO_2 is 0.3 wt% for basaltic melt at 400 MPa (Iacono-Marziano et al., 2012), making CO_2 the main driver of degassing and in many cases of magma ascent. Volatile degassing has two end-member processes (e.g., Aubaud, 2022), closed-system degassing and open-system degassing. In closed-system degassing (BED – Batch Equilibrium Degassing, often referred to as equilibrium degassing), the gas phase remains in the system and

isotopic equilibrium is maintained (e.g., Graham et al., 2018). In open-system degassing (FED – Fractional Equilibrium Degassing, often called Rayleigh distillation) exsolved CO_2 escapes from the system instantaneously (e.g., Taylor, 1986).

The carbon stable isotopic ratio in a given phase is expressed with the delta notation defined by Eq. (1) (abbreviation for Equation (1)):

$$\delta^{13}C = \left(\frac{\left(\frac{^{13}C}{^{12}C}\right)sample}{\left(\frac{^{13}C}{^{12}C}\right)reference} - 1 \right) \times 1000 \quad (1)$$

As CO_2 degasses, carbon isotope fractionation between gas and melt occurs. The fractionation factor ($\alpha_{gas\text{-}melt}$) between gas and melt is defined by Eq. (2). It has been often reported as $\Delta^{13}C_{eq}$ using an approximation (Eq. (3)), which is valid only when the absolute values of $\Delta^{13}C_{eq}$, $\delta^{13}C_{gas}$, and $\delta^{13}C_{melt}$ are all less than 10 ‰ (O'Neil, 1986; Sharp, 2017). Hereafter, we will call $1000\ln\alpha_{gas\text{-}melt}$ and the previously reported $\Delta^{13}C_{eq}$ as the fractionation coefficient.

$$\alpha_{gas\text{-}melt} = \frac{1000+\delta^{13}C_{gas}}{1000+\delta^{13}C_{melt}} \quad (2)$$

$$1000\ln\alpha_{gas\text{-}melt} \approx \Delta^{13}C_{eq} = \delta^{13}C_{gas} - \delta^{13}C_{melt} \quad (3)$$

Degassed CO_2 shows a higher $\delta^{13}C$-value compared to the melt. Several studies on carbonate, including experimental work (Chacko et al., 1991; Scheele and Hoefs, 1992; Rosenbaum, 1994; Appora, 1998; Petschnig et al., 2024) and theoretical calculations (Bottinga, 1969; Chacko et al., 1991; Deines, 2004), have shown that the fractionation coefficient decreases by 4 ‰ to 2 ‰ with increasing temperatures within the range of 700-1200 °C. The fractionation coefficient has been reported from experimental studies to be close to 0‰ for rhyolitic melt (Blank, 1993), and anywhere from +1.8 to 4.7 ‰ in basaltic melts (Javoy et al., 1978; Mattey, 1991; Mattey et al., 1990; Trull et al., 1992). The variation in the fractionation coefficient in the compositional range between rhyolite and basalts has remains unexplored.

While carbon isotope fractionation between gas and melt can be used to reconstruct the magma degassing path, the lack of constraints on the fractionation coefficient has led to inconsistency between studies. The higher $\delta^{13}C$-value of degassed CO_2 results in a subsequent decrease in the $\delta^{13}C$-value of the residual melt. As both BED and FED progress, the depletion of $\delta^{13}C$-value of CO_2 within the residual melt and coexisting gas will display a distinct evolutionary path with a steeper depletion of $\delta^{13}C$-value in FED compared to BED. For example, Pineau and Javoy (1983) proposed a two-step degassing model to explain the $\delta^{13}C$-value depletion of carbon dissolved in

MORB, with gradual $\delta^{13}C$-value depletion at higher C and steep depletion at lower C. This model has been applied to the $\delta^{13}C$-value variations in MORB (e.g., Cartigny et al., 2001) as well as arc environments (e.g., Shaw et al., 2004). However, due to the lack of agreement in the fractionation coefficient of mafic melts, $\delta^{13}C$-value of volcanic gas and basaltic rocks were modeled to generate degassing paths using either extremes or varying fractionation coefficient. For example, Mattey et al. (1989) used +1 ‰ and +4.4 ‰, Paonita et al. (2012) chose +3 ‰, while several recent studies employed +3.5 ‰ (e.g., Aubaud, 2022; Cartigny et al., 2001).

Carbon isotope fractionation in submarine volcanic glasses has been used to reconstruct pre-eruptive carbon concentration in the melt, but this estimate is highly dependent on the fractionation coefficient. The procedure measures CO_2 concentration in the gas or melt and assumes a $\delta^{13}C$-value of the initial melt (e.g., -4.5 ‰; Cartigny et al., 2001). Pre-eruptive carbon can then be calculated by modelling its degassing path (detailed calculations are provided by Cartigny et al., 2008). Estimates of Cartigny et al. (2008) (600 – 55000 ppm CO_2) and Aubaud et al. (2004) (2700 ppm CO_2) align with pre-degassed carbon estimates obtained through CO_2/Nb ratio and "popping rock", respectively. Macpherson et al. (2005) found that the Kolbeinsey Ridge melt, the northern part of the Mid-Atlantic Ridge, has a pre-eruptive CO_2 concentration (~400 ppm) lower than primitive MORB, suggesting potential degassing before equilibration at 2.7–3.0 km below the seafloor, and indicating a two-stage degassing process. All these calculations rely heavily on knowledge of the fractionation coefficient. Macpherson et al. (2005) applied two fractionation coefficient values of +2.3 ‰ and +4.5 ‰ to their calculations, resulting in a twofold difference in their resulting pre-eruptive CO_2 concentration in the melt (400 and 950 ppm, respectively).

Previous experimental studies on mafic melts yielded inconsistent CO_2 solubility and mass balance and sometimes failed to provide critical information such as melt composition or its final water content. In the first attempt to decipher fractionation coefficient, Javoy et al. (1978) reported a range of 4 – 4.6 ‰ for oceanic tholeiite. However, their dissolved CO_2 in the glass at saturation was inconsistent, ranging from 0.73 wt% to 2.56 wt% under identical conditions (750 MPa, 1280 °C). At these conditions, a CO_2 solubility of 2.56 wt% is unexpectedly high, which might imply a formation of reduced carbon formation potentially influencing carbon isotope fractionation. Two experiments using different brands of oxalic acid as a carbon source produced inconsistent CO_2 yields, 0.5 and 2.6 wt%. Finally, their step-heating measurement showed a significant contribution of low-temperature carbon released below 600 °C, which could have been from

reduced carbon form (i.e., graphite) or surface carbon contamination (Mattey et al., 1989). Mattey et al. (1990) conducted experiments on sodamelilite ($NaCaAlSi_2O_7$) and reported a smaller fractionation coefficient of 2.2 – 2.7 ‰. However, their step-heating technique only recovered 20 – 92 % of the expected carbon amount, which might have created additional kinetic isotope fractionation during the step-heating measurements. In a subsequent study, Mattey (1991) conducted an experiment on MORB melt composition obtaining results consistent with their prior research (fractionation coefficient = 1.8 – 2.2 ‰), but suffered CO_2 loss during the experiment as well. Trull et al. (1992) reported fractionation of 1.9 – 4.7 ‰ (average 3.5 ± 1.0 ‰) in experiments on MORB composition but provided limited information on their initial melt composition. The most recent experimental study, Appora (1998), investigated carbon isotope fractionation between CO_2 and carbonate melts, finding a fractionation coefficient of 3.5 ‰, which is probably not directly applicable to silicate melt.

One major challenge in interpreting previous experimental studies is the absence of available H_2O measurements on the resulting glasses, except for Blank (1993). The presence of H_2O in the melt plays a critical role in silicate structure and CO_2 behavior (e.g., Moussallam et al., 2016a; Solomatova et al., 2020; Stolper and Holloway, 1988). In one hydrous experiment conducted by Javoy et al. (1978), precise input material quantities were not provided, hindering accurate H_2O content estimation. Even though all of the experiments on mafic melt experiments (except the one above) are nominally H_2O-free, trace amounts of H_2O (a few hundred ppm to a weight percent) can still be present due to ubiquitous atmospheric water and hydrogen diffusion in experiments. Mattey (1991) and Mattey et al. (1990) have detected H_2O peaks in their infrared spectra, emphasizing the importance of measuring H_2O content in the glass, even in nominally H_2O-free experiments.

In light of these challenges, this study examines the effect of composition on the carbon isotope fractionation coefficient between gas and melt and fills the compositional gap between rhyolite and basalt. To achieve this goal, we conducted a series of experiments ranging from andesite to basanite composition at 350 – 420 MPa and 1160 – 1225°C to examine the effect of melt structure on the gas-melt isotopic fractionation coefficient.

2. Methods

2.1. Experimental Methods

The starting materials used in this study included: natural basanite from El Hierro mixed with variable amounts of SiO_2, and Al_2O_3 to produce compositions ranging from basanite to andesite (NBO series), natural basalt from Mt.Etna (Etna series), and synthetic compositions made of a four-oxide (SiO_2, Al_2O_3, MgO, and CaO) mixtures (Simple series). To ensure homogeneity and remove any initial volatiles present, all starting materials were first fused at 1300 °C in a Pt crucible at 0.1 MPa in air for 2 hours, then quenched. The retrieved glass was crushed and re-melted once more under the same conditions for an additional 2 hours. The fused glasses were examined using Fourier transform infrared spectroscopy (FTIR) to confirm that they were volatile-free (see 2.2.3).

Experiments were conducted in two internally heated pressure vessels, one at the Institut des Sciences de la Terre d'Orléans (ISTO) and the other at the American Museum of Natural History (AMNH) (Table 1). The variations in vessel size led to differences in capsule size and material quantity, with ISTO's larger vessel allowing for the use of more materials (350 mg for ISTO and 150 mg for AMNH) and larger capsules. Gold-palladium (Au_{80}-Pd_{20}) tubes (5 mm o.d. / 4.5 mm i.d. / 35 mm long for ISTO and 4.0 mm o.d. / 3.5 mm i.d. / 20 mm long for AMNH) were used in all experiments. Cut and annealed capsules were initially welded flat at one end for the ISTO experiment and triple-crimped then welded for AMNH. Then, the capsules were ultrasonically cleaned in dichloromethane for 10 minutes to remove any organic carbon that might have been present on the capsule's surface (Mattey et al., 1989) and then stored at 110 °C prior to use. The capsules were prepared by filling them with starting material, deionized water (1 – 4 wt%), and dihydrated oxalic acid ($C_2H_2O_4 \cdot 2H_2O$) (1-6 wt% of CO_2). The $\delta^{13}C$-value of the dihydrated oxalic acid used is -20.58 ‰ for the Etna series, -26.68 ‰ for the NBO and Simple series and was determined by repeated measurements with an elemental analyzer coupled isotope ratio mass spectrometer (see 2.2.2.) with a standard deviation of ± 0.14 ‰. The final welding process utilized flat welding with tungsten electrodes to minimize the introduction of additional carbon into the capsule.

The detailed experimental conditions are listed in Table 1. Pure argon was used as a pressure medium (leading to oxygen fugacities above FMQ+1, where FMQ is the fayalite-magnetite-quartz buffer; Webster and De Vivo, 2002 for AMNH; Gaillard et al., 2003 for ISTO). This high oxidation state ensured that all carbon exists in oxidized forms, the CO_2 molecular or CO_3^{2-} (Wardell et al.,

2004). Most of the experiments were conducted at superliquidus conditions, except for samples CI_IPGP_NBO_3_6 and CI_IPGP_NBO_5_2. After reaching the target P-T, the experiments were equilibrated for 18 – 24 hours. Experiments were then quenched isobarically by drop-quench at a rate of approximately 100 °C/s (Di Carlo et al., 2006).

Table 1

Conditions of IHPV experiments

Sample	Pressure (MPa)	Temperature (°C)	Duration (h)	Run at
CI_AMNH_NBO_1_3	347	1202	18	AMNH
CI_AMNH_NBO_2	348	1168	20	AMNH
CI_AMNH_NBO_2_2	350	1201	22	AMNH
CI_AMNH_NBO_3	351	1189	48	AMNH
CI_AMNH_NBO_3_1	351	1182	24	AMNH
CI_AMNH_NBO_3_2	351	1160	23	AMNH
CI_AMNH_NBO_3_4	350	1200	24	AMNH
CI_AMNH_NBO_4	349	1187	24	AMNH
CI_AMNH_NBO_5	349	1200	24	AMNH
CI_IPGP_NBO_1_2	400	1225	24	ISTO
CI_IPGP_NBO_3_6	393	1225	22	ISTO
CI_IPGP_NBO_5_2	393	1225	22	ISTO
CI_NBO_2_2	400	1225	24	ISTO
CI_NBO_3_3	400	1225	24	ISTO
ETNA-3-2	419	1200	24	ISTO

ETNA-3-2bis	419	1200	24	ISTO
ETNA-3-3	419	1200	24	ISTO
ETNA-4-1	371	1200	24	ISTO

2.2. Analytical Methods

The gas phase was extracted from the sealed capsule and analyzed first, followed by the isotopic analysis of the dissolved CO_2 in the glass using an elemental analyzer coupled to an isotope ratio mass spectrometer. The concentration of volatiles (CO_2-H_2O) and the major element composition of the glass were analyzed using FTIR and electron microprobe, respectively. The occurrence of crystals within experimental samples was checked by scanning electron microscopy (SEM).

2.2.1. $\delta^{13}C$-value analysis in the gas phase

The amount of CO_2 in the gas and its isotopic signature ($\delta^{13}C_g$) were analyzed at the Institut de Physique du Globe de Paris (IPGP), France. Post experiment, each sealed capsule was pierced under vacuum in a dedicated extraction line. After piercing, the gas released from the capsule was passed over CuO enclosed in a Pt foil to catalyze the oxidation reaction at 450 °C. This process was carried out to ensure the conversion of any CO and H_2 present to CO_2 and H_2O (although the amount of CO and H_2 was negligible). The extracted gas was then captured in a cold trap at -196 °C. After 15 minutes of trapping, any remaining gas (mostly N_2) was pumped off. CO_2 was then released by setting the temperature of the cold trap at -135 °C to retain only H_2O. CO_2 was cold trapped again and then released in a calibrated volume with a Baratron capacitance manometer to measure its total amount in the range 0-10 μmol. For larger amounts (>10 μmol), CO_2 was measured with a mercury manometer (± 5 %). The gas is finally trapped in a Pyrex® glass tube for isotopic analysis, which was performed using a dual inlet Delta Plus XP isotope ratio mass spectrometer (IRMS) equipped with a microvolume (± 0.03 ‰).

2.2.2. $\delta^{13}C$-value analysis in the glass

The isotopic signature of CO_2 dissolved in the glass ($\delta^{13}C_m$) was determined using a Costech elemental analyzer (EA) coupled with a ConFlo IV and Thermo Scientific Delta V plus isotope ratio mass spectrometer (IRMS) at Lamont−Doherty Earth Observatory. Thin glass shards were

carefully hand-picked under a microscope to avoid entrapped gas bubbles. Glass shards were then weighed on a microbalance (± 0.001 mg), placed into a 3.2 × 4 mm tin capsule, and kept in a desiccator until analysis.

The enclosed samples were dropped into a 980 °C oven and then combusted at ~1700 °C with excess oxygen (25 ml/min) over a chromium (III) oxide catalyst. Helium was used as the carrier gas (100 ml/min). Silvered cobaltous/cobaltic oxide inside the quartz combustion tube ensured the complete conversion of sample carbon to CO_2 and the removal of residual halogens or sulfur. After the separation of the CO_2 peaks through a gas chromatography (GC) column (55 °C), each sample was analyzed by IRMS.

The $\delta^{13}C_m$-values for each sample were calibrated by three-point regression using standards USGS24 ($\delta^{13}C$ = -16.04 ‰, VPDB), USGS40 ($\delta^{13}C$ = -26.77 ‰, VPDB), and USGS41 ($\delta^{13}C$ = 37.63 ‰, VPDB) with an average precision of 0.16 ‰. All measurements of carbon isotope standards agree with the accepted values reported by the United States Geological Survey (USGS). To test for instrument performance and linear drift, one standard set was analyzed for every 10 samples. The measurement error of the $\delta^{13}C$-value, calculated to be ± 0.14 ‰, was determined based on repeated measurements of the carbon source, oxalic acid.

The instrument was calibrated using acetanilide (C_8H_9NO) to determine the bulk carbon content (± 0.2 %, R^2 = 0.9999). Additional calibration was performed with a mixture of oxalic acid and SiO_2 containing 70, 20, 5, 2, 1, 0.75, 0.5, and 0.25 wt% of CO_2 (R^2 = 0.9999) to properly account for the characteristics of the glass material to be analyzed. A set of standards was inserted for each daily run. Linear regression was used to derive the calibrated total carbon content based on the true concentration of the mixture series. Based on the reproducibility of the mixture series, the error in CO_2 estimation was calculated to be ± 7.3 %.

2.2.3. Glass analysis by Fourier transform infrared spectroscopy (FTIR)

H_2O and CO_2 concentrations in the retrieved glasses were measured using a Thermo Nicolet iN10 Fourier transform infrared (FTIR) spectrometer at Lamont−Doherty Earth Observatory. The instrument was purged with dry and CO_2-scrubbed air. The measurements were made on a liquid nitrogen-cooled MCT-A detector.

Glass chips were doubly polished with alumina-coated polishing paper. Their thickness ranged from 20 to 100μm. The glass chips were washed with acetone to remove any crystal bond before

they were placed on a CaF_2 plate for measurement. Thickness was measured using the reflectance method (± 3 µm; Nichols and Wysoczanski, 2007).

Absorption spectra were collected from each sample in the 400 – 8000 cm^{-1} range with 256 scans and 1 cm^{-1} resolution in transmitted mode. The aperture size was 100 µm in width and height. To confirm the homogeneity of H_2O and CO_2 contents in the glass, a minimum of 3 spots were analyzed for each sample.

Total H_2O content was calculated using the intensity of the OH^- stretching band at around 3550 cm^{-1}. The CO_2 doublet peaks around 1515 cm^{-1} and 1435 cm^{-1} were used to determine the CO_2 concentration. Baseline correction is performed by subtracting the spectra of chemically matched devolatilized glasses (i.e., our starting compositions fused in air). The absorption coefficient of CO_2 was determined using the Na/(Na+Ca) molar ratio of the glass composition (Dixon and Pan, 1995). The absorption coefficient of H_2O was determined to be 63 L/mol/cm (Dixon et al., 1995). To calculate the glass density, both H_2O and CO_2 were taken into account (Bourgue and Richet, 2001; Lesher and Spera, 2015).

2.2.4. Electron Microprobe

Electron microprobe analyses were conducted at AMNH using a Cameca SX5-Tactis to determine the major element composition of the experimental glasses, utilizing a 15 kV accelerating voltage, a defocused beam of 10 µm, 4 nA beam current for Na (10 s count time) and 10 nA for other elements (20 s count time). Na was analyzed first in order to have a minimum of Na loss during the analysis. The instrument was calibrated using natural and synthetic mineral standards and glasses including: potassium feldspar (Al, Si, and K), rutile (Ti), fayalite (Fe), rhodonite (Mn), olivine (Mg), anorthite (Ca), jadeite (Na), and apatite (P). Ten random spots were analyzed to obtain an average value for each glass and the errors are reported as the standard deviation of the 10 repeated analyses. The samples were imaged with Scattered Electron Microscope (SEM) with Bruker Quantax Quad at AMNH.

3. Results

Quench crystals were not observed under the 500 magnifications of the microscope and SEM images (Fig. S1). IPGP_NBO_3_6 and CI_IPGP_NBO_5_2 included opaque Fe-oxides (less than 1 % in volume) that grew during the experiment (Fig. S1). Glass compositions analyzed by electron

microprobe are shown in Table 2. CO_2 dissolved in the glass (CO_{2glass}), H_2O dissolved in the glass (H_2O_{glass}), $\delta^{13}C$-value of the gas ($\delta^{13}C_g$) and glass ($\delta^{13}C_m$) are shown in Table 3. CO_{2glass} in Table 3 is measured by FTIR, except for type "Simple" (CI_NBO_2_2 and CI_NBO_3_3), in which it was obtained by EA, due to the absence of known absorption coefficient for FTIR on this Si-Al-Ca-Mg composition. CO_{2glass} measured by EA (Table S2) is in good agreement with CO_{2glass} measured by FTIR (Fig. 1). CO_{2glass} varies from 500 to 3600 ppm, increasing with the degree of depolymerization (Fig. 2). H_2O dissolved in the glass measured by FTIR varies from 1 to 3 wt%. $\delta^{13}C$-value of the gas and melt diverge from the carbon source as the depolymerization degree increases (Fig. 3). The fractionation coefficient is calculated from the $\delta^{13}C$-value of the melt and of the coexisting gas as $1000\ln\alpha_{g\text{-}m}$ (see introduction for the definition). The fractionation coefficient shows a linear relationship with composition (Fig. 4). The linear correlation derived is below:

$$1000\ln\alpha_{g\text{-}m}=2.847\times NBO/T+0.068 \ (R^2=0.74) \quad (4)$$

$$1000\ln\alpha_{g\text{-}m}=-0.087\times(SiO_2+Al_2O_3)wt\%+7.968 \ (R^2=0.74) \quad (5)$$

where NBO/T is calculated on an hydrous basis:

$$NBO/T = 2 \times \frac{X_{H_2O}+X_{K_2O}+X_{Na_2O}+X_{CaO}+X_{MgO}+X_{FeO}+X_{MnO}-X_{Al_2O_3}}{X_{SiO_2}+2\times X_{Al_2O_3}} \quad (6)$$

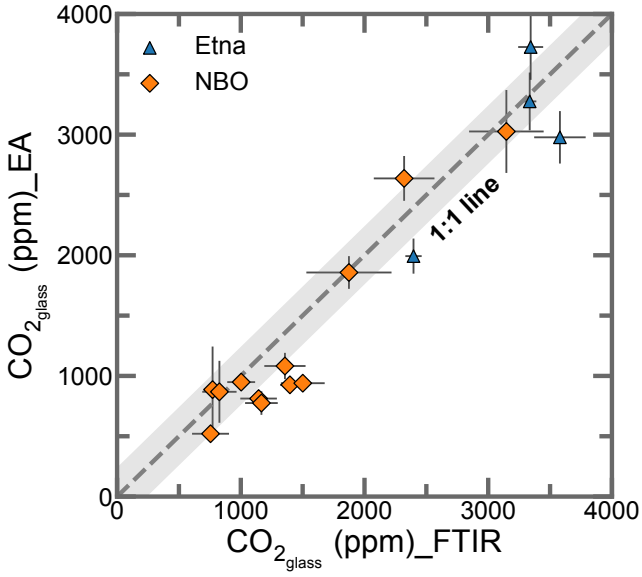

321

322 **Fig. 1.** CO_2 dissolved in the glass (CO_{2glass}) measured by EA versus FTIR in ppm. The dashed line
323 is the 1 to 1 line. Only "Etna" and "NBO" are shown on the plot, as the FTIR result of "Simple"
324 is missing due to the lack of a known absorption coefficient for this composition. Shades represent
325 the average 1-sigma deviation between two measurements. CO_2 dissolved in the glass measured
326 by FTIR and bulk CO_2 measured by EA follow a general 1 to 1 correlation, which confirms that
327 the EA measurements were not contaminated by additional surface carbon, CO_2 in gas bubbles, or
328 other suspicious reduced materials.

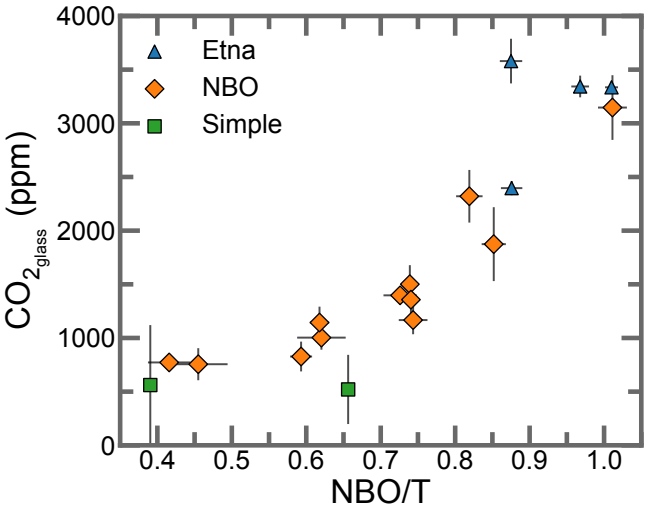

329

330 **Fig. 2.** CO_{2glass} in ppm as a function of NBO/T (non-bridging oxygens to tetrahedral cations),
331 which shows a general increase in CO_{2glass} with the depolymerization degree. CO_{2glass} is measured
332 by FTIR except "Simple" series (see result) and associated error is a standard deviation of repeated
333 measurement.

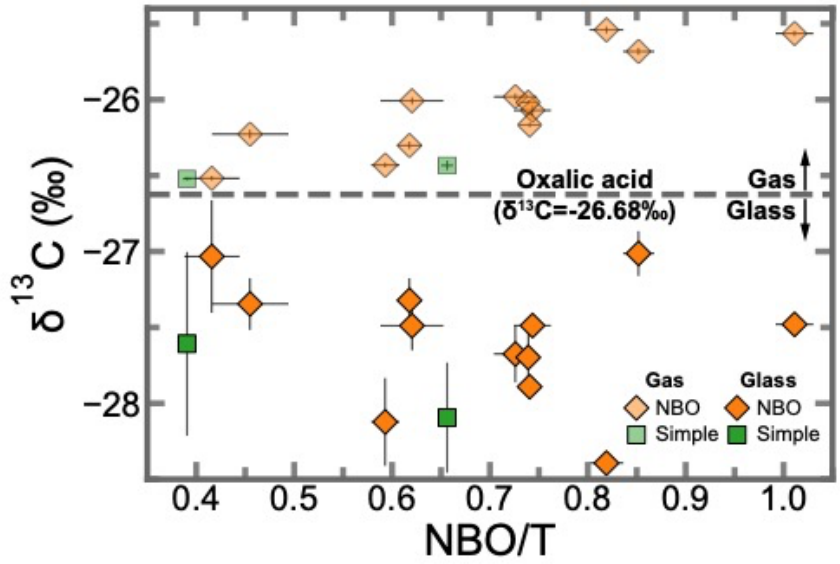

334

335 **Fig. 3.** This plot shows the $\delta^{13}C$-value of gas and glass in each experiment relative to the initial
336 $\delta^{13}C$-value of the carbon source (dashed line). Only "NBO" and "Simple" are shown on the plot,
337 since oxalic acid with a different $\delta^{13}C$-value was used for "Etna" ($\delta^{13}C$=-20.58 ‰).

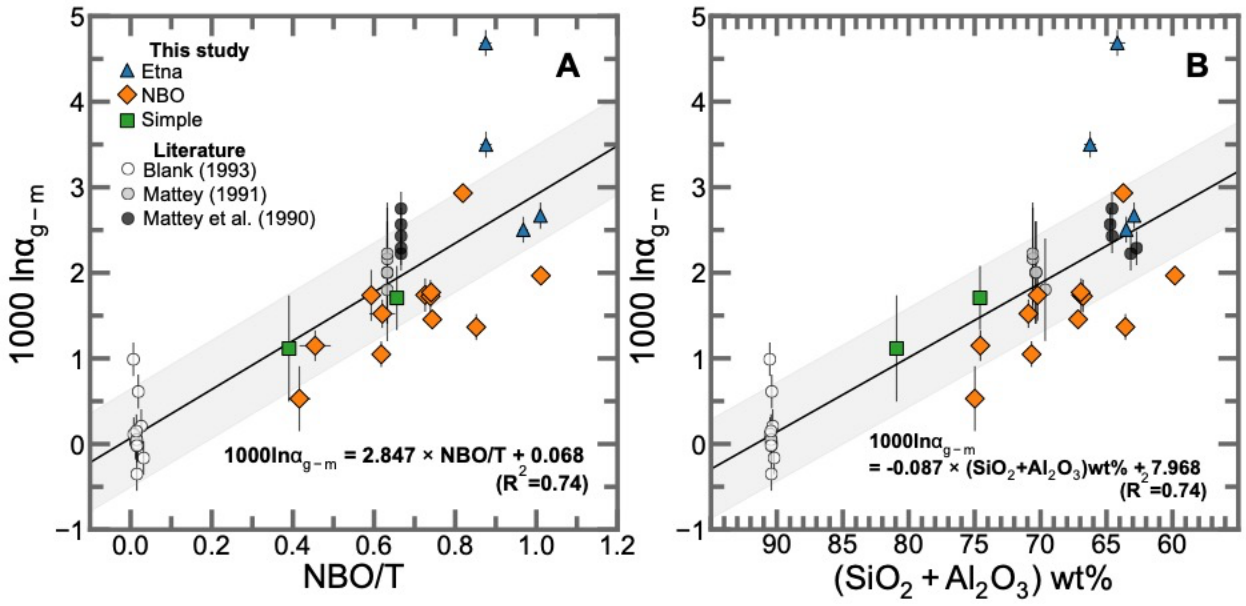

338

339 **Fig. 4** The dashed line represents a linear regression of data from our study and the literature
340 (Mattey et al., 1990; Mattey, 1991; Blank, 1993). The legend is shown in the top left corner. A)
341 NBO/T plotted against $1000\ln\alpha_{g\text{-}m}$ which represents the $\delta^{13}C$-value fractionation between gas and
342 melt. The linear regression equation shown in the bottom right corner is Eq. (4) and R^2 is 0.74. B)
343 $1000\ln\alpha_{g\text{-}m}$ is plotted as a function of network-forming elements (SiO_2+Al_2O_3) in wt%. The x-axis
344 is inverted. The regression equation in the lower right is Eq. (5) and R^2 is 0.74. The shaded area is
345 a 1-sigma error range.

Table 2

Compositions of the glass (in wt%) analyzed by electron microprobe after the experiment, normalized to a volatile-free basis. The unnormalized raw analytical sum of the averaged measurements is shown in Table S1. The values are an average of 10 repeated analyses. Standard deviations are reported in parentheses.

Sample	Type	SiO_2	TiO_2	Al_2O_3	FeO	MnO	MgO	CaO	Na_2O	K_2O	P_2O_5
CI_AMNH_NBO_1_3	NBO	57.77 (0.57)	2.73 (0.04)	18.79 (0.36)	6.86 (0.19)	0.10 (0.04)	3.48 (0.05)	6.12 (0.11)	2.47 (0.07)	1.06 (0.02)	0.63 (0.05)
CI_AMNH_NBO_2	NBO	56.18 (0.23)	3.12 (0.03)	16.96 (0.10)	8.03 (0.20)	0.12 (0.06)	3.85 (0.05)	6.85 (0.06)	2.93 (0.07)	1.29 (0.02)	0.67 (0.07)
CI_AMNH_NBO_2_2	NBO	55.00 (0.26)	3.17 (0.05)	17.96 (0.08)	7.82 (0.17)	0.12 (0.05)	3.94 (0.07)	7.07 (0.07)	2.95 (0.09)	1.27 (0.02)	0.70 (0.03)
CI_AMNH_NBO_3	NBO	52.06 (0.19)	3.61 (0.04)	17.18 (0.07)	8.76 (0.17)	0.15 (0.07)	4.55 (0.06)	8.12 (0.06)	3.31 (0.06)	1.44 (0.02)	0.82 (0.03)
CI_AMNH_NBO_3_1	NBO	51.17 (0.34)	3.58 (0.04)	17.69 (0.10)	9.25 (0.13)	0.19 (0.08)	4.50 (0.05)	8.10 (0.05)	3.31 (0.09)	1.40 (0.04)	0.81 (0.09)
CI_AMNH_NBO_3_2	NBO	51.28 (0.22)	3.60 (0.06)	17.51 (0.10)	9.39 (0.23)	0.17 (0.05)	4.47 (0.07)	8.05 (0.08)	3.34 (0.12)	1.41 (0.02)	0.78 (0.04)
CI_AMNH_NBO_3_4	NBO	51.17 (0.16)	3.56 (0.03)	17.91 (0.11)	9.11 (0.19)	0.11 (0.05)	4.50 (0.05)	8.10 (0.07)	3.31 (0.10)	1.41 (0.02)	0.81 (0.05)
CI_AMNH_NBO_4	NBO	49.03 (0.26)	3.98 (0.04)	16.18 (0.05)	10.54 (0.13)	0.19 (0.06)	4.98 (0.06)	8.90 (0.09)	3.70 (0.12)	1.64 (0.02)	0.87 (0.07)
CI_AMNH_NBO_5	NBO	45.87 (0.25)	4.51 (0.03)	15.51 (0.10)	11.37 (0.20)	0.20 (0.05)	5.58 (0.07)	10.19 (0.04)	3.98 (0.23)	1.80 (0.03)	0.99 (0.06)

CI_IPGP_NBO_1_2	NBO	57.94 (0.40)	2.67 (0.05)	18.73 (0.19)	7.06 (0.20)	0.12 (0.07)	3.30 (0.08)	5.95 (0.09)	2.53 (0.08)	1.11 (0.02)	0.59 (0.04)
CI_IPGP_NBO_3_6	NBO	54.14 (0.24)	2.62 (0.11)	17.56 (0.28)	6.89 (0.14)	0.14 (0.03)	4.31 (0.04)	8.42 (0.17)	3.65 (0.15)	1.48 (0.03)	0.78 (0.07)
CI_IPGP_NBO_5_2	NBO	48.67 (0.25)	3.60 (0.04)	16.29 (0.05)	7.28 (0.27)	0.20 (0.06)	5.55 (0.04)	10.76 (0.07)	4.58 (0.10)	1.94 (0.03)	1.12 (0.06)
CI_NBO_2_2	Simple	65.33 (0.36)	0.03 (0.01)	16.75 (0.06)	0.09 (0.06)	0.03 (0.04)	6.62 (0.09)	11.09 (0.07)	0.03 (0.01)	0.02 (0.01)	0.01 (0.01)
CI_NBO_3_3	Simple	60.37 (0.28)	0.02 (0.02)	15.45 (0.11)	0.06 (0.05)	0.03 (0.04)	8.97 (0.07)	14.99 (0.09)	0.07 (0.02)	0.02 (0.00)	0.02 (0.02)
ETNA-3-2	Etna	48.80 (0.25)	1.68 (0.08)	16.66 (0.15)	9.85 (0.07)	0.19 (0.03)	6.43 (0.08)	10.66 (0.12)	3.29 (0.19)	1.91 (0.03)	0.54 (0.04)
ETNA-3-2bis	Etna	48.68 (0.17)	1.66 (0.05)	16.27 (0.14)	10.63 (0.08)	0.18 (0.03)	6.35 (0.05)	10.53 (0.09)	3.30 (0.14)	1.87 (0.07)	0.53 (0.06)
ETNA-3-3	Etna	49.22 (0.61)	1.66 (0.05)	16.32 (0.16)	9.87 (0.28)	0.17 (0.05)	6.37 (0.06)	10.64 (0.09)	3.29 (0.12)	1.89 (0.04)	0.56 (0.07)
ETNA-4-1	Etna	51.17 (0.44)	1.70 (0.05)	17.17 (0.16)	5.97 (0.20)	0.18 (0.04)	6.67 (0.05)	11.15 (0.12)	3.45 (0.24)	1.97 (0.05)	0.57 (0.04)

346

Table 3

Final CO_2 and H_2O concentrations in the glass, $\delta^{13}C$-value in the glass and gas phases, and resulting isotopic fractionation coefficient. 1-sigma error is shown.

Sample	CO_{2glass} (ppm)	±	H_2O_{glass} (wt%)	±	$\delta^{13}C_{glass}$ (‰)	±	$\delta^{13}C_{gas}$ (‰)	±	$1000\ln\alpha_{g\text{-}m}$	±
CI_AMNH_NBO_1_3	755	149	2.52	0.44	-27.35	0.17	-26.23	0.03	1.15	0.18

CI_AMNH_NBO_2	1003	113	2.92	0.35	-27.49	0.16	-26.01	0.03	1.52	0.17
CI_AMNH_NBO_2_2	1144	148	3.01	0.13	-27.32	0.15	-26.30	0.03	1.05	0.15
CI_AMNH_NBO_3	1167	132	2.89	0.19	-27.49	0.07	-26.07	0.03	1.46	0.08
CI_AMNH_NBO_3_1	1397	80	2.68	0.22	-27.68	0.19	-25.98	0.02	1.74	0.20
CI_AMNH_NBO_3_2	1501	177	2.76	0.05	-27.70	0.19	-26.02	0.02	1.73	0.19
CI_AMNH_NBO_3_4	1357	167	2.94	0.09	-27.89	0.06	-26.17	0.02	1.77	0.06
CI_AMNH_NBO_4	1874	344	2.33	0.14	-27.01	0.15	-25.68	0.03	1.37	0.16
CI_AMNH_NBO_5	3147	301	2.23	0.15	-27.48	0.01	-25.57	0.02	1.97	0.02
CI_IPGP_NBO_1_2	772	71	2.12	0.32	-27.03	0.37	-26.52	0.02	0.53	0.38
CI_IPGP_NBO_3_6	827	139	1.98	0.11	-28.12	0.29	-26.43	0.02	1.74	0.30
CI_IPGP_NBO_5_2	2320	245	1.66	0.15	-28.39	0.05	-25.54	0.03	2.93	0.06
CI_NBO_2_2	561	559	1.36	0.03	-27.61	0.61	-26.52	0.01	1.12	0.62
CI_NBO_3_3	520	322	1.56	0.03	-28.09	0.37	-26.43	0.03	1.71	0.38
ETNA-3-2	3343	101	2.66	0.06	-22.70	0.15	-20.25	0.02	2.50	0.15
ETNA-3-2bis	3335	54	2.81	0.02	-22.19	0.15	-19.58	0.02	2.67	0.15
ETNA-3-3	3580	208	1.73	0.07	-24.23	0.15	-19.65	0.03	4.69	0.16
ETNA-4-1	2396	66	2.84	0.08	-22.31	0.15	-18.88	0.03	3.50	0.16

4. Discussion

4.1. Data reliability

A critical consideration is whether the experiments reached equilibrium. First, we stress that the experimental systems remained entirely closed with no evidence of open system behavior or leakage. The recovered capsules did not show any weight loss after the experiment (Table S2). Extracted gas was mostly CO_2 (17-276 μmole) with minor traces of H_2O (background level), as

355 expected (Table S2). The recovered glasses exhibited consistent homogeneity, with a relative
356 standard deviation below 5 % in 10 repeated analyses, regardless of their location within the
357 sample (Table 2). Previous experiments under P-T-X conditions similar to ours demonstrated that
358 they reached equilibrium by "reversal test", i.e. first equilibrating at high pressure and then re-
359 equilibrating at lower pressure for 20 minutes to 2.5 hours (Mattey, 1991; Dixon et al., 1995).
360 Reversal experiments showed CO_2 solubility, $\delta^{13}C$-value of the glass and gas results consistent
361 with forward experiments, indicating that a duration of 20 minutes at 1400 °C is sufficient to reach
362 equilibrium. We are, therefore, confident that the duration of our experiment (18 – 48 hours)
363 allowed us to reach elemental and isotopic equilibrium for carbon.
364 Some of the primary challenges in analyzing the $\delta^{13}C$-value in experimental glasses are the
365 presence of sub-solidus carbonate precipitates, CO_2 gas exsolution in the bubbles during quench,
366 or carbon adsorption (Mattey, 1991; Macpherson et al., 1999). Several results support the
367 successful recovery of $\delta^{13}C$-value in the glass. No solid carbonate phases were observed under the
368 microscope and with the SEM. Isobaric drop quenching was used to ensure rapid quenching and
369 minimize post-experiment CO_2 exsolution from the melt to the gas bubble (e.g., Paillat et al., 1992).
370 Few large bubbles were observed in the recovered glasses, due to volatile saturation, but they were
371 easily avoidable by selecting thin shards under the microscope. Although the presence of
372 submicroscopic gas bubbles cannot be excluded, the strong correspondence between dissolved
373 CO_2 contents measured by FTIR and EA (Fig. 1), strongly suggests that the contributions of the
374 solid carbonate, gas bubbles, and surface carbon are minor compared to the predominant dissolved
375 CO_2 in the glass.
376 The question of whether a reduced form of carbon existed in the gas or melt is significant due
377 to its potential to substantially impact solubility, fractionation properties, and carbon interactions
378 with the melt structure. Pure argon was used as the pressure medium for the experiment, which is
379 estimated to induce an oxygen fugacity above FMQ+1 in the IHPV (Webster and De Vivo, 2002;
380 Gaillard et al., 2003). This environment allows carbon to dissolve in the silicate melt in its oxidized
381 form (CO_3^{2-} or CO_2 molecular) (e.g, Wardell et al., 2004). We didn't observe any reduced carbon
382 species (e.g., CH_4, CO) in the FTIR spectra, and the good agreement between CO_{2glass} measured
383 by FTIR and EA (Fig.1) suggests the absence of reduced carbon species in the glass. Moreover,
384 our CO_2 solubilities are comparable with those predicted by CO_2 solubility models at the given P-

T-X (Iacono-Marziano et al., 2012) (Fig. S2), corroborating the absence of reduced carbon as well as other major carbon species besides CO_3^{2-} in the glass.

4.2. Compositional effect

Our experiments, conducted at 1160 – 1225°C and 350 – 420 MPa, investigate the $\delta^{13}C$-value fractionation coefficient between gas and silicate melt ($1000\ln\alpha_{g\text{-}m}$) over a range of compositions from andesitic basalt to basanite. Fig. 4 illustrates the relationships between melt composition and $1000\ln\alpha_{g\text{-}m}$ derived from both our study and the literature (Mattey et al., 1990; Mattey, 1991; Blank, 1993). In reviewing previous experiments, we have excluded the measurement from Javoy et al. (1978) and Trull et al. (1992) because of the absence of melt composition and H_2O_{glass} information, which significantly affects silicate melt structures. In addition, the analyses of Javoy et al. (1978) included low-temperature carbon from the step-heating method for $\delta^{13}C_{glass}$, possibly originating from surface carbon or contamination (e.g., Mattey et al., 1989). In CO_2-sodamelilite experiments (Mattey et al., 1990), we excluded the results that showed carbonate precipitation during the experiment to focus solely on the fractionation between CO_2 and silicate melt. Given these considerations, we have excluded these measurements from further examination.

Due to the complexity of the various carbon species in the silicate melt and the species-specific fractionation behavior, the gas-melt fractionation factor can be expressed as the sum of the mole fractions by species multiplied by each fractionation factor (Deines, 2004). In the gas, oxidized experimental conditions allowed CH_4 and CO to be excluded and only CO_2 to be included (e.g., Gaillard et al., 2003; Wardell et al., 2004; Webster and De Vivo, 2002). CO_2 is dissolved in the silicate melt as either carbonate ion (CO_3^{2-}) or CO_2 molecular (Brey and Green, 1976; Mysen et al., 1976; Blank and Brooker, 1994), CO_3^{2-}/CO_2 ratios decreasing with the polymerization of the melt (detailed in discussion later in this section). Carbon isotopic fractionation in silicate melt is therefore a combination of two fractionations between gas and melt: (1) CO_2 gas-CO_2 molecular in the melt and (2) CO_2 gas-CO_3^{2-} in the melt.

It should be noted that equilibrium between volatile gases and silicate melt is achieved by diffusion processes. Reaction of the CO_2 molecular-CO_2 gas is expected to dominate over CO_3^{2-}-CO_2 gas in the diffusion process (e.g., Spickenbom et al., 2010). The diffusion coefficient of bulk CO_2 in silicate melts is nearly invariant over a wide range of compositions (e.g., Sierralta et al., 2002). This is because the increase in CO_2 molecular diffusivity from rhyolite to basalt melts is

countered by a concurrent decrease in the fraction of CO_2 dissolved as CO_2 molecular with respect to that dissolved as CO_3^{2-}(Nowak et al., 2004). The diffusion coefficient of CO_2 is one order of magnitude (tholeiite) to four orders of magnitude (rhyolite) higher than that of CO_3^{2-} (Nowak et al., 2004; Spickenbom et al., 2010). The activation energy of CO_3^{2-} for diffusion is also more than twice as high (80.6 kJ/mol for CO_3^{2-} and 34.5 kJ/mol for CO_2 molecular), regardless of the composition range (Guillot and Sator, 2011).

In addition, CO_3^{2-} is much more strongly bonded to the silicate structure than CO_2 molecular, in other words, it has a lower mobility in the melt and between the melt and gas phase. The CO_2 molecular and CO_3^{2-} are bound to non-bridging oxygen (NBO, bound to one network former or to a network modifier cation) and bridging oxygen (BO, bound to two network formers) in the silicate structure, rather than forming a true carbonate complex with cations (Guillot and Sator, 2011; Moussallam et al., 2016b). According to molecular dynamics simulation for carbon in silicate melts, the distance from the carbon to the nearest oxygen is more than twice as short for CO_3^{2-} (1.25A) than for the CO_2 molecular (2.65A) (Guillot and Sator, 2011).

While CO_3^{2-} exhibits limited mobility due to its lower diffusivity and stronger bonding, a rapid interconversion between the CO_2 molecular and CO_3^{2-} has been observed, surpassing the rate of CO_2 transport in the melt. This is demonstrated by the experiment showing a constant CO_3^{2-}/CO_2 ratio throughout diffusion profiles measured by FTIR (Sierralta et al., 2002). Molecular dynamics simulations further support this observation, indicating that every diffusing CO_2 molecular into the melt undergoes numerous interconversions before exiting from the melt (Guillot and Sator, 2011). The homogenous equilibrium of the CO_2 gas-CO_3^{2-} reaction is maintained during the diffusion process in the silicate melt. Consequently, the carbon exchange between the melt and the gas is controlled by the CO_2 molecular, involving the conversion of CO_3^{2-} to CO_2 molecular in the melt rather than direct diffusion of CO_3^{2-} out of the melt.

The $\delta^{13}C$-value fractionation between CO_2 gas and CO_2 molecular in the melt appears to be negligible, as shown by the experiment with a rhyolitic composition that contains only CO_2 molecular in the melt (Fig. 3). Given the similar geometry of CO_2 gas and CO_2 molecular, minimal fractionation is expected. The close correspondence in antisymmetric stretching frequencies observed in IR and NMR studies between the CO_2 molecular in glass (2350cm^{-1}, 125 ppm) and CO_2 gas (2348 cm^{-1}, 124.2 ppm) further supports the similar geometry of the molecular structure between the two (e.g., Kohn et al., 1991). In addition, the comparable activation energy between

447 the molecular CO_2 and Ar suggests that molecular CO_2 behaves as an inert molecule which has no
448 isotopic fractionation between gas and melt at equilibrium (e.g., Marty and Humbert, 1997).
449 In contrast, during CO_3^{2-}-CO_2 molecular conversion in the melt, ^{13}C is enriched in the CO_2
450 molecular rather than in CO_3^{2-}. This is explained by isotope fractionation rules (Grootes et al.,
451 1969), which is the preference of the heavy isotope ^{13}C for lower coordination numbers and
452 symmetric molecules, CO_2. Considering the lower mobility of CO_3^{2-} and the rapid conversion
453 between the two species in the melt (see reasoning above), we expect the isotope fractionation to
454 occur primarily between the CO_3^{2-} and CO_2 molecular in the melt, rather than between CO_3^{2-} and
455 CO_2 gas. Consequently, the bulk fractionation may be indicative of CO_3^{2-}/CO_2 species ratio in the
456 melt.
457 Infrared spectroscopy studies of quenched silicate glasses have shown that CO_2 exists
458 exclusively as the CO_2 molecular in rhyolite (Fogel and Rutherford, 1990) and as CO_3^{2-} in basalt
459 (Fine and Stolper, 1986; Shishkina et al., 2014). In intermediate compositions, infrared
460 spectroscopy studies showed that dissolved CO_2 in the glass exists as a combination of both with
461 a systematic decrease in CO_3^{2-}/CO_2 ratio towards the felsic composition (Brey, 1976; Fogel and
462 Rutherford, 1990; King and Holloway, 2002). However, the speciation in quenched glasses is not
463 an accurate representation of that of silicate melts. Experimental studies (Morizet et al., 2001;
464 Nowak et al., 2003), molecular dynamic studies (Guillot and Sator, 2011; Moussallam et al.,
465 2016b), and a synchrotron in situ infrared study (Konschak and Keppler, 2014) all show that, whilst
466 it may not be preserved in the glass, even depolymerized melts such as basalts contain non-
467 negligeable amounts of molecular CO_2 at high temperature.
468 Eq. (4) and (5) are calibrated from NBO/T = 0 to 1, covering most major melt compositions at
469 the earth's surface and we interpret these relationships as the result of dissolved carbon speciation
470 going from entirely CO_2 molecular in rhyolite (NBO/T≈0) to predominantly CO_3^{2-} in alkalic basalt
471 and basanite (NBO/T≈1). At NBO/T > 1 however, we expect the relationship to stabilize and
472 remain constant as the majority of the carbon will be dissolved as CO_3^{2-} by then and the CO_3^{2-}/CO_2
473 ratio won't increase significantly with further depolymerisation. This interpretation is consistent
474 with the experimental results of Petschnig et al., (2024) on nephelinite-CO_2 fractionation at 1175°C
475 and 0.3 GPa (Fig. 5).
476 H_2O induces depolymerization of the silicate melt, increasing NBO/T (e.g., Stolper, 1982). An
477 increase in fractionation coefficient is simply expected with H_2O addition, however, the paucity of

data on the effect of the H_2O content on the carbon speciation hinders a conclusive understanding of its effect on carbon isotope fractionation. Furthermore, the limited range of H_2O content (1.4 – 3.0 wt%) in this study makes it difficult to accurately estimate its effect on carbon isotope fractionation.

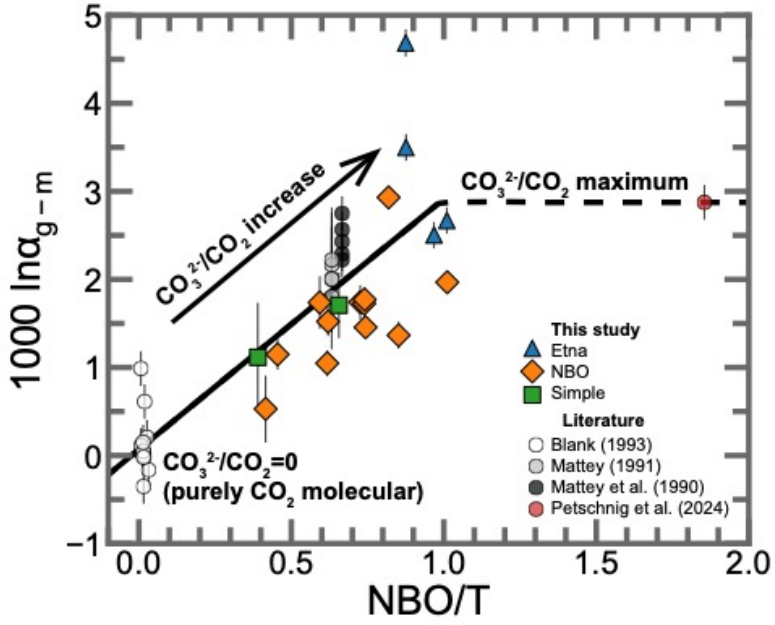

Fig. 5. This plot illustrates the carbon isotope fractionation coefficient ($1000\ln\alpha_{g\text{-}m}$) between CO_2 gas and carbon dissolved in silicate melts, integrating results from our study with literature data from rhyolite (Blank, 1993), MORB (Mattey, 1991), sodamelilite (Mattey et al., 1990), and nephelinite (Petschnig et al., 2024). The graph depicts a scenario where carbon is present in rhyolite only as CO_2 molecular, while the CO_3^{2-}/CO_2 ratio increases with depolymerization of the melt. It also highlights the limitation of CO_3^{2-} incorporation into silicate melts, indicating the attainment of the maximum CO_3^{2-}/CO_2 ratio that silicate melts can have around NBO/T=1. The solid line represents Eq. (4), while the dashed line extends from the point of Petschnig et al. (2024).

4.3. Temperature effect

Experimental results and literature data are plotted against $10^6/T^2$ in Fig. 6. Theoretical calculation studies on pure carbonate system predict a decrease in fractionation coefficient with increasing temperature, as expected for an equilibrium process (Chacko et al., 1991; Deines, 2004; Petschnig et al., 2024). This trend is also expected from the changes in species ratios in the melt. A decrease in temperature and an increase in pressure is expected to result in an increase in the

CO_3^{2-}/CO_2 ratio (Fine and Stolper, 1985; Guillot and Sator, 2011; Konschak and Keppler, 2014; Morizet et al., 2015), which should lead to an expected increase in fractionation coefficient. However, over the temperature range of our study and previous experiments (Mattey et al., 1990; Mattey, 1991), no trend in fractionation coefficient with temperature at constant composition is discernible.

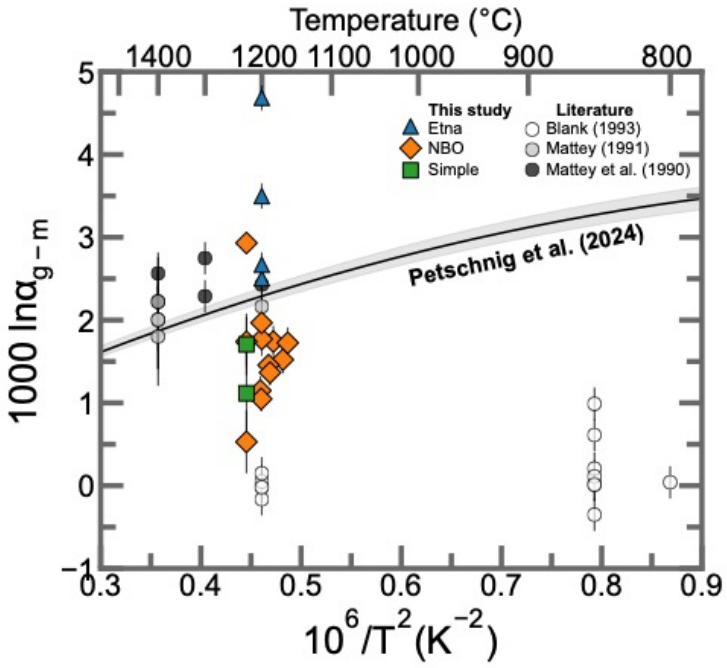

Fig. 6. Isotopic fractionation versus $10^6/T^2$ in K^{-2} for this study and literature data. The solid black line represents the carbonate-CO_2 gas fractionation line derived by Petschnig et al. (2024). The shaded area is an error estimated by Petschnig et al. (2024).

4.4. Application

The equation derived from this study allows the calculation of fractionation coefficients. Here, comparisons are made with fractionation coefficients derived from natural samples. Graham et al. (2018) estimated the fractionation coefficient in MORB from the East Pacific Rise (EPR). Assuming closed-system degassing, a linear regression slope between $\delta^{13}C$-value and CO_2 fraction of vesicle yields a fractionation coefficient of 3.3 ‰ (± 0.5 ‰). Using Eq. (4) and (5), fractionation coefficient of 2.3 ‰ was calculated based on its basalt composition (Goss et al., 2010). The higher fractionation coefficient in Graham et al. (2018) suggests the potential involvement of open-system degassing, resulting in greater carbon isotope depletion. In the extensively degassed central Lau Basin, most $\delta^{13}C$-values and CO_2 concentrations in the glass data were consistent with a fractional

equilibrium degassing (FED) line plotted with a fractionation coefficient of 2.3 ‰ (Macpherson and Mattey, 1994), which is comparable to our calculation of 2.2 ‰ (melt composition and H_2O from Kent et al., 2002 and Pearce et al., 1994).

As the carbon isotope fractionation coefficient varies with melt composition, it should be expected to change as magma evolves during fractional crystallization. To investigate the effect of magma evolution on $\delta^{13}C$-value changes during degassing, we performed fractional crystallization simulation using MELTS (Fig. 7). The initial setting was Etna melt inclusion composition (Kamenetsky et al., 2007), 600 MPa, and 1180 °C. The SiO_2 content ranges from 44 wt% to 52 wt%, resulting in a decrease in fractionation coefficient from 3.3 ‰ to 1.1 ‰. Both the BED and FED show a steeper decrease in $\delta^{13}C$-value during the early stages of crystallization, with smaller isotope fractionation as magma evolves. A higher $\delta^{13}C$-value difference between gas-melt in depolymerized melt further suggests that observing a higher $\delta^{13}C$-value in volcanic gas may not necessarily indicate an increased source $\delta^{13}C$-value but could reflect mafic recharge of the magma chamber.

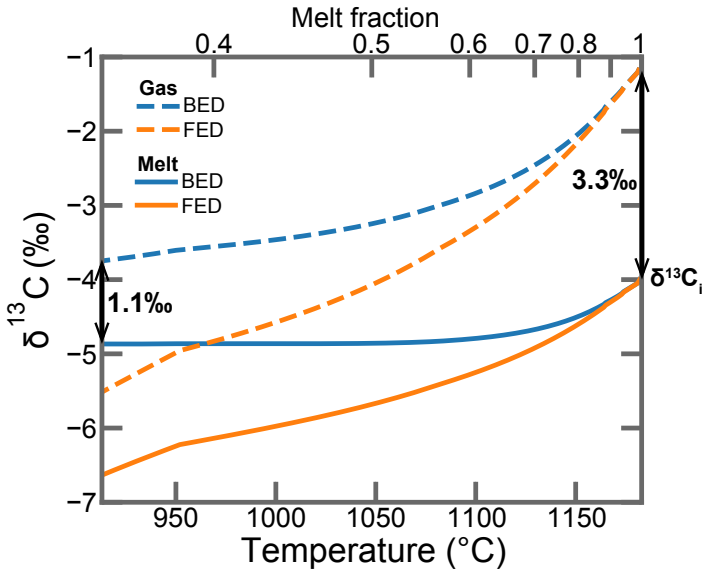

Fig. 7. A simulation result from rhyolite-MELTS (v.1.2.0) that shows the evolution of isotopic compositions ($\delta^{13}C$) for gas and melt phases under isobaric conditions at 600MPa. The starting composition is from melt inclusions from Etna volcano (Reference) and the temperature is 1200°C. The fractionation coefficient changes from 3.3 ‰ to 1.1 ‰ as the melt composition changes. The $\delta^{13}C_i$-value is set to be -4 ‰. The dashed line represents the gas $\delta^{13}C$-value and the solid line represents the melt $\delta^{13}C$-value. BED and FED refer to Batch and Fractional Equilibrium Degassing, respectively. The temperature and corresponding melt fraction remaining in the system are plotted on the bottom and top axes, respectively.

The $\delta^{13}C$-value of carbon dissolved in the melt ($\delta^{13}C_m$) provides valuable insights into identifying the carbon source and determining the initial carbon isotope ratio and carbon concentration by tracing degassing pathways. $\delta^{13}C_m$ is influenced by a combination of 1) BED, 2) FED, 3) kinetic fractionation, 4) carbonate precipitation from the melt, 5) mixing with organic sediment, and 6) assimilation with surrounding carbonate (Fig. 8).

$$\delta^{13}C_m = M\times\{\delta^{13}C_i + \Delta^{13}C_{eq}(F-1) + \Delta^{13}C_{eq}\ln(F/F_0) + \Delta^{13}C_{kin}\ln(F/F_0) + \Delta^{13}C_{carb}(F/F_0-1)\} + S\times\delta^{13}C_{org} + L\times\delta^{13}C_{lime} \quad (7)$$

$\delta^{13}C_i$, the initial $\delta^{13}C$-value, may differ from the source; most mantle values are estimated in a range of -4 ‰ to -6 ‰ (Cartigny et al., 1998). $\Delta^{13}C_{eq}$ (fractionation coefficient) can be derived from Eq. (4) in this study, taking into account the melt composition of each system. F is the remaining CO_2 fraction in the silicate melt relative to the initial, while F_0 is the fraction at which Rayleigh distillation or FED or carbonate precipitation begins. BED and Rayleigh distillation induce a decrease in $\delta^{13}C$-values with different slopes. Conversely, kinetic fractionation is a diffusive mass-dependent reaction ($\Delta^{13}C_{kin}$=-8.7 ‰; Javoy and Pineau, 1991), resulting in the gas having a smaller $\delta^{13}C$-value than the melt, and consequently increasing $\delta^{13}C_m$. Carbonate precipitation from the melt has minimal effect on $\delta^{13}C$-values due to the near-zero fractionation ($\Delta^{13}C_{carb}$=0.39 ‰; Petschnig et al., 2024) between silicate melt and precipitated carbonatite. Organic sediment significantly reduces $\delta^{13}C$-values, whereas marine limestone typically has values close to 0‰ ($\delta^{13}C_{org}$ =-30 ‰ and $\delta^{13}C_{lime}$ =0 ‰; Sano and Marty, 1995). M, S, and L are the mole fractions of silicate melts, organic sediment and limestone (or carbonate), respectively with M+S+L=1 (Sano and Marty, 1995). Understanding these processes enables accurate interpretation of $\delta^{13}C$-value for carbon dynamics.

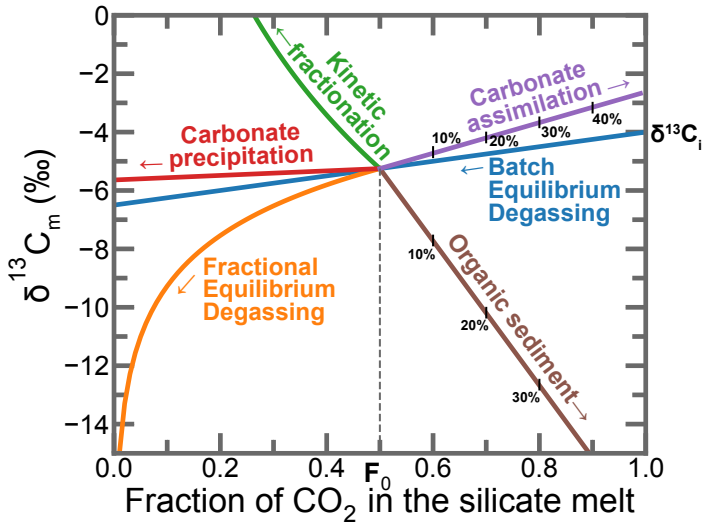

Fig. 8. Semi-quantitative assessment of magmatic processes that can affect the $\delta^{13}C$ of the melt ($\delta^{13}C_m$). The fractionation coefficient used here is 2.5 ‰. In a closed system, Batch Equilibrium Degassing (BED) occurs (blue). At point F_0, Fractional Equilibrium Degassing (FED) (orange) follows, resulting in a significant decrease in $\delta^{13}C$-value. Kinetic fractionation (green) may occur during degassing, potentially increasing $\delta^{13}C$. The precipitation of carbonatite (red) from the melt has minimal impact on $\delta^{13}C$. The $\delta^{13}C_m$ is affected by mixing with carbonate (purple) or organic sediment (brown), as indicated by the percentage of mixed carbonate or sediment represented by the tick on its line.

5. Conclusions

We conducted experiments at 350 – 420 MPa and 1160 – 1225 °C across a range of compositions from basanite to andesite to derived carbon isotope fractionation coefficient between CO_2 gas and carbon dissolved in the silicate melt.

We found a positive linear correlation between the carbon fractionation coefficient and the composition or the degree of depolymerization of the melt.

$$1000\ln\alpha_{gas\text{-}melt}=2.847\times NBO/T+0.068\ (R^2=0.74)$$

and

$$1000\ln\alpha_{g\text{-}m}=-0.087\times(SiO_2+Al_2O_3)wt\%+7.968\ (R^2=0.74)$$

These equations allow the calculation of the carbon isotope fractionation coefficient for the most commonly occurring silicate melts ranging from basanite to rhyolite. At NBO/T > 1 we expect the isotope fractionation coefficient to remain constant at ~2.9 ‰ as we hypothesize that the ratio of

588 CO_3^{2-}/CO_2 dissolved in the melt is the key parameter behind this relationship. Carbon isotopic
589 fractionation might hence offer a window into carbon speciation in natural melts.
590 Melt temperature and H_2O could be of secondary importance to determine the carbon isotope
591 fractionation coefficient compared to melt composition, but their effects should be investigated
592 further.
593
594 **Acknowledgments**
595 This study is funded by FORED (Foundation for Overseas Resources Development)
596 scholarship program. We would like to thank Celine Martin for her assistance with the microprobe
597 analysis. Special thanks are extended to Wei Huang for her valuable contributions to the elemental
598 analyzer analysis.
599 **Data Availability**
600 Data are available through Mendeley Data at
601 https://data.mendeley.com/preview/vp6ngrjzdy?a=d27af8c4-7fbb-4b02-b771-43723c5d328f
602
603 **CRediT authorship contribution statement**
604 **Hyunjoo Lee:** Conceptualization, Data curation, Investigation, Methodology, Supervision,
605 Validation, Visualization, Writing – original draft, Writing – review & editing. **Yves Moussallam:**
606 Conceptualization, Formal Analysis, Funding acquisition, Methodology, Project administration,
607 Resources, Supervision, Validation, Writing – review & editing. **Cyril Aubaud:** Conceptualization,
608 Formal Analysis, Methodology, Resources, Validation, Writing – review & editing. **Giada Iacono-**
609 **Marziano:** Conceptualization, Formal Analysis, Methodology, Resources, Validation, Writing –
610 review & editing. **Keiji Hammond:** Methodology, Resources, Validation. **Denton Ebel:**
611 Resources, Supervision, Writing – review & editing, Validation.
612
613 **Appendix A. Supplementary Material**
614 The supplementary material includes Figure S1, which presents SEM images of the
615 experimental glasses, Figure S2, providing a comparison between CO_2 dissolved in the glass and
616 the expected solubility using a model. Table S1 is unnormalized analytical total of major
617 composition data, and Table S2 details the mass difference before and after each experiment,
618 CO_{2glass} measurements by elemental analyzer, and the extracted amounts of CO_2 and H_2O gas.

Declaration of generative AI and AI-assisted technologies in the writing process

During the preparation of this work the authors used DeepL in order to correct grammatical error and improve readability. After using this tool/service, the authors reviewed and edited the content as needed and takes full responsibility for the content of the publication.

References

Andersen T. and Neumann E.-R. (2001) Fluid inclusions in mantle xenoliths. *Lithos* **55**, 301–320.

Appora G. (1998) Etude experimentale du fractionnement isotopique du carbone et de l'oxygene dans les systemes CO_2-carbonates liquides : application au contexte carbonatitique. Paris Diderot University - Paris 7.

Aubaud C. (2022) Carbon stable isotope constraints on CO_2 degassing models of ridge, hotspot and arc magmas. *Chemical Geology* **605**, 120962.

Aubaud C., Pineau F., Jambon A. and Javoy M. (2004) Kinetic disequilibrium of C, He, Ar and carbon isotopes during degassing of mid-ocean ridge basalts. *Earth and Planetary Science Letters* **222**, 391–406.

Blank J. G. (1993) An experimental investigation of the behavior of carbon dioxide in rhyolitic melt. Ph.D. Thesis, California Institute of Technology.

Blank J. G. and Brooker R. A. (1994) Chapter 5. Experimental studies of carbon dioxide in silicate melts: solubility, speciation, and stable carbon isotope behavior. In *Volatiles in Magmas* (eds. M. R. Carroll and J. R. Holloway). De Gruyter. pp. 157–186.

640 Bottinga Y. (1969) Calculated fractionation factors for carbon and hydrogen isotope exchange in
641 the system calcite-carbon dioxide-graphite-methane-hydrogen-water vapor. *Geochimica*
642 *et Cosmochimica Acta* **33**, 49–64.

643 Bourgue E. and Richet P. (2001) The effects of dissolved CO_2 on the density and viscosity of
644 silicate melts: a preliminary study. *Earth and Planetary Science Letters* **193**, 57–68.

645 Brey G. (1976) CO_2 solubility and solubility mechanisms in silicate melts at high pressures.
646 *Contr. Mineral. and Petrol.* **57**, 215–221.

647 Brey G. P. and Green D. H. (1976) Solubility of CO_2 in olivine melilitite at high pressures and
648 role of CO_2 in the earth's upper mantle. *Contr. Mineral. and Petrol.* **55**, 217–230.

649 Brooker R. A., Kohn S. C., Holloway J. R. and McMillan P. F. (2001) Structural controls on the
650 solubility of CO_2 in silicate melts. *Chemical Geology* **174**, 225–239.

651 Cartigny P., Harris J. W. and Javoy M. (1998) Eclogitic Diamond Formation at Jwaneng: No
652 Room for a Recycled Component. *Science* **280**, 1421–1424.

653 Cartigny P., Jendrzejewski N., Pineau F., Petit E. and Javoy M. (2001) Volatile (C, N, Ar)
654 variability in MORB and the respective roles of mantle source heterogeneity and
655 degassing: the case of the Southwest Indian Ridge. *Earth and Planetary Science Letters*
656 **194**, 241–257.

657 Cartigny P., Pineau F., Aubaud C. and Javoy M. (2008) Towards a consistent mantle carbon flux
658 estimate: Insights from volatile systematics (H_2O/Ce, δD, CO_2/Nb) in the North Atlantic
659 mantle (14° N and 34° N). *Earth and Planetary Science Letters* **265**, 672–685.

660 Chacko T., Mayeda T. K., Clayton R. N. and Goldsmith J. R. (1991) Oxygen and carbon isotope
661 fractionations between CO_2 and calcite. *Geochimica et Cosmochimica Acta* **55**, 2867–
662 2882.

663 Dasgupta R. and Hirschmann M. M. (2010) The deep carbon cycle and melting in Earth's
664 interior. *Earth and Planetary Science Letters* **298**, 1–13.

665 Deines P. (2004) Carbon isotope effects in carbonate systems. *Geochimica et Cosmochimica*
666 *Acta* **68**, 2659–2679.

667 Dixon J. E. (1997) Degassing of alkalic basalts. *American Mineralogist* **82**, 368–378.

668 Dixon J. E., Edward M. Stolper, and John R. Holloway (1995) An Experimental Study of Water
669 and Carbon Dioxide Solubilities in Mid-Ocean Ridge Basaltic Liquids. Part I: Calibration
670 and Solubility Models. *Journal of Petrology* **36**, 1607–1631.

671 Dixon J. E. and Pan V. (1995) Determination of the molar absorptivity of dissolved carbonate in
672 basanitic glass. *American Mineralogist* **80**, 1339–1342.

673 Fine G. and Stolper E. (1986) Dissolved carbon dioxide in basaltic glasses: concentrations and
674 speciation. *Earth and Planetary Science Letters* **76**, 263–278.

675 Fine G. and Stolper E. (1985) The speciation of carbon dioxide in sodium aluminosilicate
676 glasses. *Contr. Mineral. and Petrol.* **91**, 105–121.

677 Fogel R. A. and Rutherford M. J. (1990) The solubility of carbon dioxide in rhyolitic melts; a
678 quantitative FTIR study. *American Mineralogist* **75**, 1311–1326.

679 Gaillard F., Malki M., Iacono-Marziano G., Pichavant M. and Scaillet B. (2008) Carbonatite
680 Melts and Electrical Conductivity in the Asthenosphere. *Science* **322**, 1363–1365.

681 Gaillard F., Pichavant M. and Scaillet B. (2003) Experimental determination of activities of FeO
682 and Fe_2O_3 components in hydrous silicic melts under oxidizing conditions. *Geochimica et*
683 *Cosmochimica Acta* **67**, 4389–4409.

684 Graham D. W., Michael P. J. and Rubin K. H. (2018) An investigation of mid-ocean ridge
685 degassing using He, CO_2, and $\delta^{13}C$ variations during the 2005–06 eruption at 9°50′N on
686 the East Pacific Rise. *Earth and Planetary Science Letters* **504**, 84–93.

687 Grootes P. M., Mook W. G. and Vogel J. C. (1969) Isotopic fractionation between gaseous and
688 condensed carbon dioxide. *Z. Physik* **221**, 257–273.

689 Guillot B. and Sator N. (2011) Carbon dioxide in silicate melts: A molecular dynamics
690 simulation study. *Geochimica et Cosmochimica Acta* **75**, 1829–1857.

691 Iacono-Marziano G., Morizet Y., Le Trong E. and Gaillard F. (2012) New experimental data and
692 semi-empirical parameterization of H_2O–CO_2 solubility in mafic melts. *Geochimica et*
693 *Cosmochimica Acta* **97**, 1–23.

694 Ida Di Carlo, Michel Pichavant, Silvio G. Rotolo, and Bruno Scaillet (2006) Experimental
695 Crystallization of a High-K Arc Basalt: the Golden Pumice, Stromboli Volcano (Italy).
696 *Journal of Petrology* **47**, 1317–1343.

Ionov D. A., Dupuy C., O'Reilly S. Y., Kopylova M. G. and Genshaft Y. S. (1993) Carbonated peridotite xenoliths from Spitsbergen: implications for trace element signature of mantle carbonate metasomatism. *Earth and Planetary Science Letters* **119**, 283–297.

Jaques A. L., O'Neill H. St. C., Smith C. B., Moon J. and Chappell B. W. (1990) Diamondiferous peridotite xenoliths from the Argyle (AK1) lamproite pipe, Western Australia. *Contr. Mineral. and Petrol.* **104**, 255–276.

Javoy M. and Pineau F. (1991) The volatiles record of a "popping" rock from the Mid-Atlantic Ridge at 14°N: chemical and isotopic composition of gas trapped in the vesicles. *Earth and Planetary Science Letters* **107**, 598–611.

Javoy M., Pineau F. and Iiyama I. (1978) Experimental determination of the isotopic fractionation between gaseous CO_2 and carbon dissolved in tholeiitic magma: A preliminary study. *Contr. Mineral. and Petrol.* **67**, 35–39.

Jendrzejewski N., Trull T. W., Pineau F. and Javoy M. (1997) Carbon solubility in Mid-Ocean Ridge basaltic melt at low pressures (250–1950 bar). *Chemical Geology* **138**, 81–92.

Kamenetsky V. S., Pompilio M., Métrich N., Sobolev A. V., Kuzmin D. V. and Thomas R. (2007) Arrival of extremely volatile-rich high-Mg magmas changes explosivity of Mount Etna. *Geol* **35**, 255.

Kent A. J. R., Peate D. W., Newman S., Stolper E. M. and Pearce J. A. (2002) Chlorine in submarine glasses from the Lau Basin: seawater contamination and constraints on the composition of slab-derived fluids. *Earth and Planetary Science Letters* **202**, 361–377.

King P. L. and Holloway J. R. (2002) CO_2 solubility and speciation in intermediate (andesitic) melts: the role of H_2O and composition. *Geochimica et Cosmochimica Acta* **66**, 1627–1640.

Kohn S. C., Brooker R. A. and Dupree R. (1991) ^{13}C MAS NMR: A method for studying CO_2 speciation in glasses. *Geochimica et Cosmochimica Acta* **55**, 3879–3884.

Konschak A. and Keppler H. (2014) The speciation of carbon dioxide in silicate melts. *Contrib Mineral Petrol* **167**, 998.

Le Voyer M., Kelley K. A., Cottrell E. and Hauri E. H. (2017) Heterogeneity in mantle carbon content from CO_2-undersaturated basalts. *Nature Communications* **8**, 14062.

Lesher C. E. and Spera F. J. (2015) Thermodynamic and Transport Properties of Silicate Melts and Magma. In *The Encyclopedia of Volcanoes* Elsevier. pp. 113–141.

Macpherson C. G., Hilton D. R., Mertz D. F. and Dunai T. J. (2005) Sources, degassing, and contamination of CO_2, H_2O, He, Ne, and Ar in basaltic glasses from Kolbeinsey Ridge, North Atlantic. *Geochimica et Cosmochimica Acta* **69**, 5729–5746.

Macpherson C. G., Hilton D. R., Newman S. and Mattey D. P. (1999) CO_2, $^{13}C/^{12}C$ and H_2O variability in natural basaltic glasses: a study comparing stepped heating and ftir spectroscopic techniques. *Geochimica et Cosmochimica Acta* **63**, 1805–1813.

Macpherson C. and Mattey D. (1994) Carbon isotope variations of CO_2 in Central Lau Basin basalts and ferrobasalts. *Earth and Planetary Science Letters* **121**, 263–276.

736 Marty B. and Humbert F. (1997) Nitrogen and argon isotopes in oceanic basalts. *Earth and*
737 *Planetary Science Letters* **152**, 101–112.

738 Mattey D. P. (1991) Carbon dioxide solubility and carbon isotope fractionation in basaltic melt.
739 *Geochimica et Cosmochimica Acta* **55**, 3467–3473.

740 Mattey D. P., Exley R. A. and Pillinger C. T. (1989) Isotopic composition of CO_2 and dissolved
741 carbon species in basalt glass. *Geochimica et Cosmochimica Acta* **53**, 2377–2386.

742 Mattey D. P., Taylor W. R., Green D. H. and Pillinger C. T. (1990) Carbon isotopic fractionation
743 between CO_2 vapour, silicate and carbonate melts: an experimental study to 30 kbar.
744 *Contr. Mineral. and Petrol.* **104**, 492–505.

745 Michael P. J. and Graham D. W. (2015) The behavior and concentration of CO_2 in the suboceanic
746 mantle: Inferences from undegassed ocean ridge and ocean island basalts. *Lithos* **236–**
747 **237**, 338–351.

748 Morizet Y., Kohn S. C. and Brooker R. A. (2001) Annealing experiments on CO_2-bearing jadeite
749 glass: an insight into the true temperature dependence of CO_2 speciation in silicate melts.
750 *Mineral. mag.* **65**, 701–707.

751 Morizet Y., Vuilleumier R. and Paris M. (2015) A NMR and molecular dynamics study of CO_2-
752 bearing basaltic melts and glasses. *Chemical Geology* **418**, 89–103.

753 Moussallam Y., Morizet Y. and Gaillard F. (2016a) H_2O–CO_2 solubility in low SiO_2-melts and
754 the unique mode of kimberlite degassing and emplacement. *Earth and Planetary Science*
755 *Letters* **447**, 151–160.

Moussallam Y., Florian P., Corradini D., Morizet Y., Sator N., Vuilleumier R., Guillot B., Iacono-Marziano G., Schmidt B. C. and Gaillard F. (2016b) The molecular structure of melts along the carbonatite–kimberlite–basalt compositional joint: CO_2 and polymerisation. *Earth and Planetary Science Letters* **434**, 129–140.

Mysen B. O., Eggler D. H., Seitz M. G. and Holloway J. R. (1976) Carbon dioxide in silicate melts and crystals; Part I, Solubility measurements. *American Journal of Science* **276**, 455–479.

Nichols A. R. L. and Wysoczanski R. J. (2007) Using micro-FTIR spectroscopy to measure volatile contents in small and unexposed inclusions hosted in olivine crystals. *Chemical Geology* **242**, 371–384.

Nowak M., Porbatzki D., Spickenbom K. and Diedrich O. (2003) Carbon dioxide speciation in silicate melts: a restart. *Earth and Planetary Science Letters* **207**, 131–139.

Nowak M., Schreen D. and Spickenbom K. (2004) Argon and CO_2 on the race track in silicate melts: A tool for the development of a CO_2 speciation and diffusion model. *Geochimica et Cosmochimica Acta* **68**, 5127–5138.

O'Neil J. R. (1986) Chapter 1. Theoretical and experimental aspects of isotopic fractionation. In *Stable Isotopes in High Temperature Geological Processes* (eds. J. W. Valley, H. P. Taylor, and J. R. O'Neil). De Gruyter. pp. 1–40.

Paillat O., Elphick S. C. and Brown W. L. (1992) The solubility of water in $NaAlSi_3O_8$ melts: a re-examination of Ab-H_2O phase relationships and critical behaviour at high pressures. *Contr. Mineral. and Petrol.* **112**, 490–500.

Paonita A., Caracausi A., Iacono-Marziano G., Martelli M. and Rizzo A. (2012) Geochemical evidence for mixing between fluids exsolved at different depths in the magmatic system of Mt Etna (Italy). *Geochimica et Cosmochimica Acta* **84**, 380–394.

Pearce J. A., Ernewein M., Bloomer S. H., Parson L. M., Murton B. J. and Johnson L. E. (1994) Geochemistry of Lau Basin volcanic rocks: influence of ridge segmentation and arc proximity. *SP* **81**, 53–75.

Pearson D. G., Boyd F. R., Haggerty S. E., Pasteris J. D., Field S. W., Nixon P. H. and Pokhilenko N. P. (1994) The characterisation and origin of graphite in cratonic lithospheric mantle: a petrological carbon isotope and Raman spectroscopic study. *Contr. Mineral. and Petrol.* **115**, 449–466.

Petschnig P., Schmidt M. W., Kueter N., Sartori G. and Bernasconi S. M. (2024) An almost universal CO_2-CO_3^{2-} carbon isotope fractionation function for high temperatures. *Earth and Planetary Science Letters* **627**, 118552.

Pineau F. and Javoy M. (1983) Carbon isotopes and concentrations in mid-oceanic ridge basalts. *Earth and Planetary Science Letters* **62**, 239–257.

Rosenbaum J. M. (1994) Stable isotope fractionation between carbon dioxide and calcite at 900°C. *Geochimica et Cosmochimica Acta* **58**, 3747–3753.

Saal A., Hauri E., Langmuir C. H. and Perfit M. (2002) Vapour undersaturation in primitive mid-ocean-ridge basalt and the volatile content of Earth's upper mantle. *Nature* **419**, 451.

796 Sano Y. and Marty B. (1995) Origin of carbon in fumarolic gas from island arcs. *Chemical*
797 *Geology* **119**, 265–274.

798 Scheele N. and Hoefs J. (1992) Carbon isotope fractionation between calcite, graphite and CO_2:
799 an experimental study. *Contrib Mineral Petrol* **112**, 35–45.

800 Sharp Z. (2017) Principles of Stable Isotope Geochemistry, 2nd Edition.

801 Shaw A. M., Hilton D. R., Macpherson C. G. and Sinton J. M. (2004) The CO_2-He-Ar-H_2O
802 systematics of the manus back-arc basin: resolving source composition from degassing
803 and contamination effects. *Geochimica et Cosmochimica Acta* **68**, 1837–1855.

804 Shishkina T. A., Botcharnikov R. E., Holtz F., Almeev R. R., Jazwa A. M. and Jakubiak A. A.
805 (2014) Compositional and pressure effects on the solubility of H_2O and CO_2 in mafic
806 melts. *Chemical Geology* **388**, 112–129.

807 Sierralta M., Nowak M. and Keppler H. (2002) The influence of bulk composition on the
808 diffusivity of carbon dioxide in Na aluminosilicate melts. *American Mineralogist* **87**,
809 1710–1716.

810 Solomatova N., Caracas R. and Cohen R. (2020) Carbon Speciation and Solubility in Silicate
811 Melts. In *Geophysical Monograph Series* (eds. C. E. Manning, J. Lin, and W. L. Mao).
812 Wiley. pp. 179–194.

813 Spickenbom K., Sierralta M. and Nowak M. (2010) Carbon dioxide and argon diffusion in
814 silicate melts: Insights into the CO_2 speciation in magmas. *Geochimica et Cosmochimica*
815 *Acta* **74**, 6541–6564.

816 Stolper E. (1982) The speciation of water in silicate melts. *Geochimica et Cosmochimica Acta*
817 **46**, 2609–2620.

818 Stolper E. and Holloway J. R. (1988) Experimental determination of the solubility of carbon
819 dioxide in molten basalt at low pressure. *Earth and Planetary Science Letters* **87**, 397–
820 408.

821 Taylor B. E. (1986) Chapter 7. Magmatic volatiles: Isotopic variation of C, H, and S. In *Stable*
822 *Isotopes in High Temperature Geological Processes* (eds. J. W. Valley, H. P. Taylor, and J.
823 R. O'Neil). De Gruyter. pp. 185–226.

824 Trull T. W., Pineau F., Bottinga Y. and Javoy M. (1992) CO_2 bubble growth and $^{13}C/^{12}C$ isotopic
825 fractionation in basaltic melt. *Eos (Washington, D.C.)* **73**, 348.

826 Wardell L. J., Kyle P. R. and Chaffin C. (2004) Carbon dioxide and carbon monoxide emission
827 rates from an alkaline intra-plate volcano: Mt. Erebus, Antarctica. *Journal of Volcanology*
828 *and Geothermal Research* **131**, 109–121.

829 Webster J. D. and De Vivo B. (2002) Experimental and modeled solubilities of chlorine in
830 aluminosilicate melts, consequences of magma evolution, and implications for exsolution
831 of hydrous chloride melt at Mt. Somma-Vesuvius. *American Mineralogist* **87**, 1046–
832 1061.

833 Yoshino T., McIsaac E., Laumonier M. and Katsura T. (2012) Electrical conductivity of partial
834 molten carbonate peridotite. *Physics of the Earth and Planetary Interiors* **194–195**, 1–9.

835

Supplementary Material

'Carbon isotope fractionation between CO_2 and carbon in silicate melts at high temperature'

Hyunjoo Lee, Yves Moussallam, Cyril Aubaud, Giada Iacono-Marziano, Keiji Hammond, and Denton Ebel

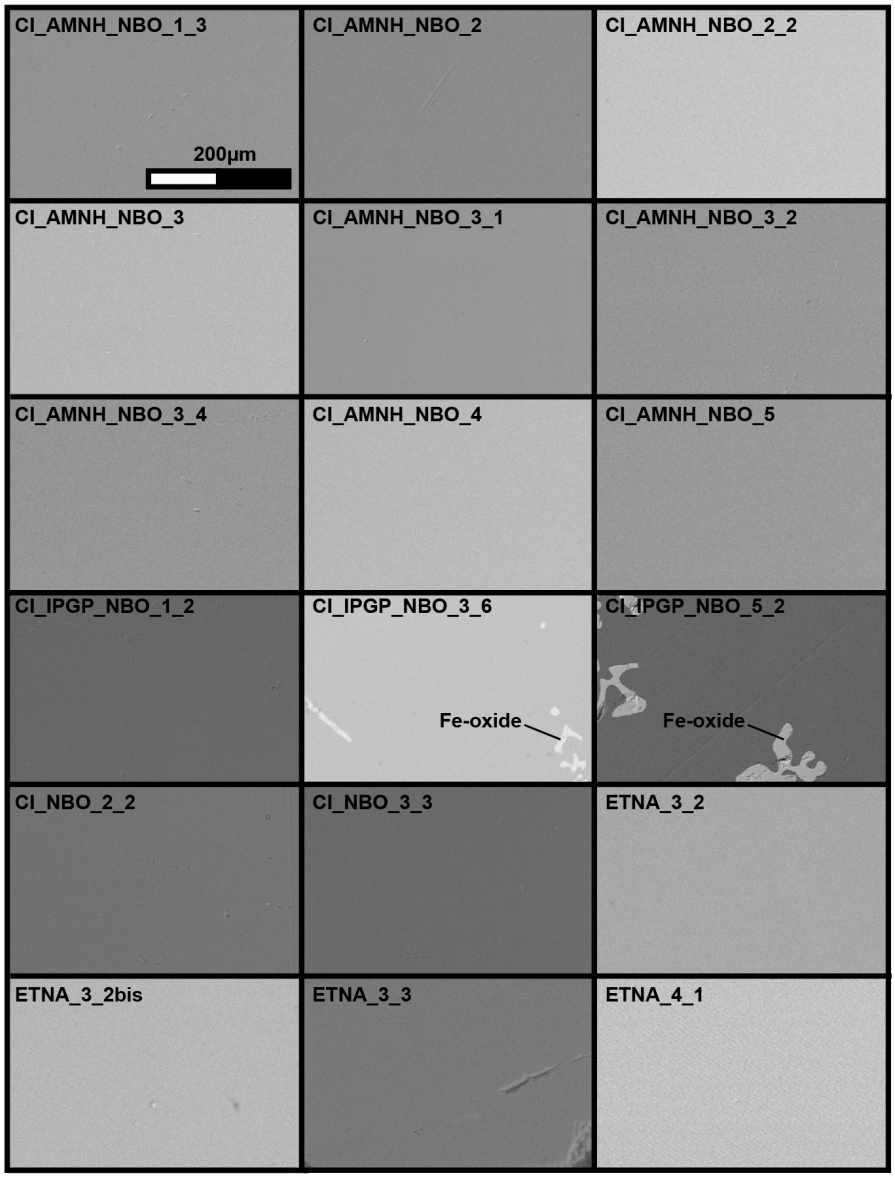

Fig. S1. Representative Scanning Electron Microscope (SEM) images taken at the AMNH (American Museum of Natural History). Sample ID is shown at top right. The scale is the same for all the images. Except for CI_IPGP_NBO_3_6 and CI_IPGP_NBO_5_2, all samples are crystal-free glass.

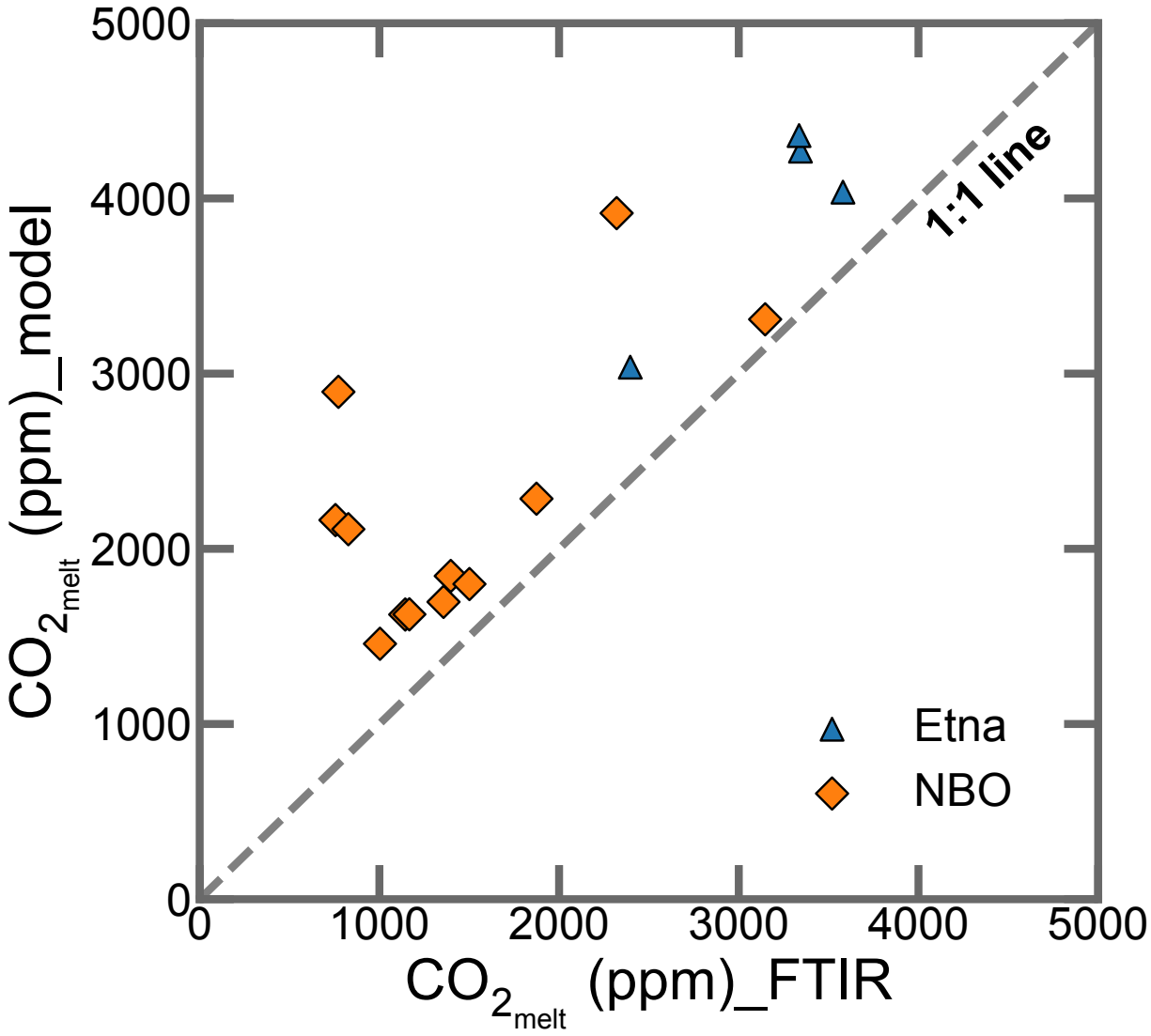

Fig. S2. CO_2 that dissolved in the glass modeled by Iacono-Marziano et al., (2012) versus measured by FTIR. Error is given by the model for y-axix error and by one sigma of repeated analysis for x-axis. Dashed line is 1 to 1 line.

Table S1

Raw result of major compositions of the glass (in wt%) analyzed by electron microprobe after the experiment. The values are an average of 10 repeated analyses.

Sample	Type	SiO_2	TiO_2	Al_2O_3	FeO	MnO	MgO	CaO	Na_2O	K_2O	P_2O_5	Total
CI_AMNH_NBO_1_3	NBO	56.44	2.67	18.35	6.70	0.10	3.40	5.97	2.42	1.03	0.62	97.7
CI_AMNH_NBO_2	NBO	54.72	3.04	16.52	7.82	0.12	3.75	6.67	2.86	1.26	0.65	97.4
CI_AMNH_NBO_2_2	NBO	53.56	3.08	17.49	7.61	0.12	3.84	6.88	2.87	1.24	0.68	97.4
CI_AMNH_NBO_3	NBO	50.54	3.50	16.68	8.50	0.14	4.42	7.88	3.22	1.40	0.80	97.1
CI_AMNH_NBO_3_1	NBO	49.72	3.48	17.19	8.99	0.18	4.38	7.87	3.22	1.36	0.78	97.2
CI_AMNH_NBO_3_2	NBO	49.89	3.50	17.03	9.13	0.16	4.35	7.83	3.25	1.37	0.76	97.3
CI_AMNH_NBO_3_4	NBO	49.72	3.46	17.40	8.85	0.10	4.37	7.87	3.22	1.37	0.79	97.1
CI_AMNH_NBO_4	NBO	47.67	3.87	15.73	10.24	0.18	4.84	8.65	3.60	1.60	0.85	97.2
CI_AMNH_NBO_5	NBO	44.13	4.34	14.92	10.93	0.20	5.37	9.80	3.83	1.73	0.95	96.2
CI_IPGP_NBO_1_2	NBO	56.57	2.59	16.50	6.89	0.12	3.23	5.81	2.23	1.09	0.56	95.6
CI_IPGP_NBO_3_6	NBO	53.54	2.59	17.36	6.82	0.14	4.26	8.32	3.61	1.46	0.77	98.9
CI_IPGP_NBO_5_2	NBO	47.31	3.50	15.83	7.08	0.20	5.40	10.46	4.45	1.89	1.09	97.2
CI_NBO_2_2	Simple	64.76	0.03	16.61	0.09	0.03	6.56	11.00	0.03	0.02	0.01	99.1
CI_NBO_3_3	Simple	59.70	0.02	15.29	0.06	0.03	8.88	14.84	0.07	0.02	0.02	98.9
ETNA-3-2	Etna	47.85	1.64	16.34	9.66	0.19	6.31	10.45	3.22	1.87	0.53	98.1
ETNA-3-2bis	Etna	47.77	1.63	15.97	10.43	0.17	6.23	10.33	3.23	1.84	0.52	98.1
ETNA-3-3	Etna	48.87	1.65	16.21	9.80	0.17	6.33	10.57	3.26	1.87	0.56	99.3
ETNA-4-1	Etna	49.95	1.66	16.76	5.83	0.17	6.51	10.88	3.37	1.92	0.56	97.6

Table S2

Mass changes of the capsule before and after the experiment, CO_2 measured by elemental analyzer (EA) in ppm, and extracted gas µmoles of CO_2 and H_2O.

Sample	Before experiment (g)	[a]After experiment (g)	CO_{2glass}_EA (ppm)	CO_{2glass}_EA ±	CO_{2gas} (µmol)	H_2O_{gas} (µmol)
CI_AMNH_NBO_1_3	1.02673	1.0278	521	[b]38	26.3	4.9
CI_AMNH_NBO_2	0.99981	0.99992	949	[b]69	20.3	4.6
CI_AMNH_NBO_2_2	1.01559	1.0161	812	[b]59	29.2	8.1
CI_AMNH_NBO_3	0.97511	0.9748	775	[c]98	21	2.6
CI_AMNH_NBO_3_1	0.9958	0.996	926	[c]53	23.9	0.9
CI_AMNH_NBO_3_2	0.9872	0.98728	940	[b]69	22.2	6.8
CI_AMNH_NBO_3_4	0.97737	0.9774	1082	[c]109	23.9	6.5
CI_AMNH_NBO_4	1.01072	1.01074	1857	[b]136	19.9	4
CI_AMNH_NBO_5	0.99472	0.99484	3026	[c]344	17.5	5.8
CI_IPGP_NBO_1_2	2.1682	2.1685	887	[c]357	55.9	4.3
CI_IPGP_NBO_3_6	2.2008	2.2013	868	[c]257	49.8	3.4
CI_IPGP_NBO_5_2	2.2285	2.2291	2637	[b]186	44.4	8.8
CI_NBO_2_2	2.2202	2.2234	561	[c]559	74.5	2.6
CI_NBO_3_3	2.1489	2.149	520	[c]322	75	8.3
ETNA-3-2	1.2146	1.2145	3726	[b]272	214	1.26
ETNA-3-2bis	1.2913	1.2911	3276	[b]239	276	1.18
ETNA-3-3	1.2684	1.2685	2978	[b]217	54	0
ETNA-4-1	1.147	1.1474	1993	[b]145	174	20.57

[a]Mass gain may occur by reaction with capsule and Pt thermocouple.

[b]Due to the limited amount of samples, there was a lack of repeated measurement. The analytical error of EA, 7.3% of the yielded value, was estimated as an error.

[c]Error is one sigma of repeated measurements